Catalysis Today 175 (2011) 603–609

Contents lists available at ScienceDirect

Catalysis Today

journal homepage: www.elsevier.com/locate/cattod

Nanosized Ag/α-MnO_2 catalysts highly active for the low-temperature oxidation of carbon monoxide and benzene

Qing Ye[a,*], Jiansheng Zhao[a], Feifei Huo[a], Juan Wang[a], Shuiyuan Cheng[a], Tianfang Kang[a], Hongxing Dai[b,**]

[a] *Department of Environmental Science, College of Environmental and Energy Engineering, Beijing University of Technology, Pingleyuan No. 100, Beijing 100124, China*
[b] *Laboratory of Catalysis Chemistry and Nanoscience, Department of Chemistry and Chemical Engineering, College of Environmental and Energy Engineering, Beijing University of Technology, Beijing 100124, China*

ARTICLE INFO

Article history:
Received 14 October 2010
Received in revised form 25 February 2011
Accepted 6 April 2011
Available online 10 May 2011

Keywords:
Nanosized alpha-MnO_2 supported silver catalyst
Low-temperature reducibility
Synergistic action
Carbon monoxide oxidation
Volatile organic compound combustion

ABSTRACT

Nanosized α-MnO_2-supported silver catalysts (xAg/*nano*-MnO_2, x = 0–10.0 wt%) were prepared by the incipient wetness impregnation method and characterized by means of numerous analytical techniques. Catalytic activities of the materials were evaluated for the oxidation of CO and benzene. It is shown that the loading of silver on *nano*-MnO_2 could significantly modify the catalytic activities and the catalytic performance of xAg/*nano*-MnO_2 strongly depended upon the Ag loading, among which 5Ag/*nano*-MnO_2 performed the best for the addressed reactions. The excellent performance of 5Ag/*nano*-MnO_2 was associated with the highly dispersed Ag, good low-temperature reducibility, and synergism at the interface of Ag and MnO_2 nanodomains.

1. Introduction

Catalytic oxidation of carbon monoxide is of considerable interest due to its relevance in many industrial applications, such as gas purification in CO_2 lasers, CO sensors, air-purification devices for respiratory protection, and pollution control devices for reducing industrial and environmental emissions [1]. Most of volatile organic compounds (VOCs) emitted from transportation and industrial activities are harmful to the atmospheric environment and human health [2,3]. Therefore, it is of significance to eliminate the VOCs [4]. The conventional incineration of organic pollutants usually requires high temperatures (>1000 °C), resulting in a rise in energy consumption. Catalytic oxidation of VOCs, however, has been generally accepted to be one of the most effective pathways for the destruction of VOCs at lower temperatures (<500 °C). Such a catalytic strategy possesses advantages of high feasibility, low operation cost, and high destruction efficiency [5]. The catalyst employed is a key issue determining the effectiveness of catalytic oxidation technology.

In the past years, a number of materials, including supported noble metals (Pt, Pd, Rh, and Au) [6–8] and base transition-metal (Cr, Co, Cu, Ni, and Mn) oxides [6,9,10], have been used as catalyst for the combustion of VOCs. The former are highly active at lower temperatures, but their applications are limited due to the high cost and involved problems related to sintering, volatility, and susceptibly poisoning tendency [6,11,12]. Hence, there is an urgent need to develop cheaper and active catalysts that exhibit high thermal stability and great resistance to poisoning.

Bulk and/or supported manganese oxides have long been used as an active catalyst for the oxidation of carbon monoxide, methane, and hydrocarbons [13]. Since a single-component catalyst is usually hard to rival a precious metal catalyst, attempts for enhancing catalytic activity have been made by combining two or more transition-metal elements. For example, Mn–Fe composite oxides showed a higher activity than the zeolite-supported Pt material in catalyzing the oxidation of oxygen-containing organic compounds [14]. Loading a small amount of gold nanoparticles on manganese oxide (i.e., Au/MnO_x) could give rise to a significant enhancement in catalytic activity for the oxidation of CO [15] and alcohol [16].

Although silver is not a good oxidation catalyst in most cases, it can be utilized as an active component of catalysts for some deep or partial oxidation. It has been demonstrated that supported silver catalysts showed good catalytic performance for the selective oxidation of ethylene to ethylene oxide [17], the oxi-

---

[*] Corresponding author. Tel.: +86 10 6739 1659; fax: +86 10 6739 1983.
[**] Corresponding author. Tel.: +86 10 6739 6118; fax: +86 10 6739 1983.
E-mail addresses: yeqing@bjut.edu.cn (Q. Ye), hxdai@bjut.edu.cn (H. Dai).

0920-5861/$ – see front matter © 2011 Elsevier B.V. All rights reserved.
doi:10.1016/j.cattod.2011.04.008

dation of acetone and pyridine [18], and the oxidation of VOCs [19]. To the best of our knowledge, no reports on the use of nanosized MnO_2-supported Ag as catalyst for benzene combustion have been seen in the literature. Recently, we have prepared numerous MnO_2-supported transition-metal catalysts and found these materials performed well in the combustion of some typical VOCs. Herein, we report the preparation, characterization, and catalytic properties of nanosized Ag/MnO_2 with various Ag loadings for the complete oxidation of carbon monoxide and benzene.

2. Experimental

2.1. Catalyst preparation

Alpha manganese oxide was synthesized by mild reduction of aqueous solution of $KMnO_4$ (0.12 mol/L) with maleic acid ($C_4H_4O_4$, 0.040 mol/L) at a molar ratio of $KMnO_4/C_4H_4O_4 = 3$ at room temperature (RT). The resulting dark brown gel was kept in air at RT for 24 h, and then filtered and washed with deionized water for several times until pH = 7. After being dried at 110 °C for about 20 h, the solid was calcined in air at a ramp of 1 °C/min from RT to 450 °C and maintained at this temperature for 3 h. The resulting α-MnO_2 sample was denoted as *nano*-MnO_2.

A certain amount of $AgNO_3$ powders was dissolved in 15 mL of deionized water to generate an $AgNO_3$ solution (0.037, 0.115, 0.195, 0.279 or 0.412 mol/L). 6 g of *nano*-MnO_2 powders was impregnated with the above $AgNO_3$ aqueous solution under stirring for 24 h. An appropriate amount of 0.5 mol/L $NaBH_4$ solution ($NaBH_4/Ag^+$ molar ratio = 3/1) was added dropwise to the mixed aqueous solution containing $AgNO_3$ and *nano*-MnO_2 under stirring for 1 h, in which most of the silver ions were reduced to metallic silver. Finally, the mixture was in turn filtered, washed with deionized water, dried at 100 °C for 24 h, and calcined in air at a ramp of 1 °C/min from RT to 450 °C and maintained at this temperature for 3 h. The obtained samples were denoted as *x*Ag/*nano*-MnO_2 with $x = 1.0$, 3.0, 5.0, 7.0, and 10.0 wt%, respectively.

2.2. Catalyst characterization

The X-ray diffraction (XRD) patterns of the samples were recorded on a Bruker-AXS D8 Advance powder diffractometer by using Cu K_α radiation ($\lambda = 0.15406$ nm) at a voltage and current of 50 kV and 30 mA, respectively. Transmission electron microscopy (TEM) was employed to take the TEM images of the samples on a TecnaiG2F20 U-TWIN (America FEI) operated at 200 kV. N_2 adsorption–desorption isotherms were measured at −196 °C on a Micromeritics ASAP 2010 instrument. Prior to the experiments, the samples were degassed at 200 °C for 2 h. The surface areas of the samples were determined by the Brunauer–Emmett–Teller (BET) method. XPS spectra of the *x*Ag/*nano*-MnO_2 samples were recorded on an ESCA-LAB-220i spectrometer, using Al K_α radiation at a voltage and current of 20 kV and 30 mA, respectively. The binding energies of the Ag 3d, Mn 2p, and O 1s were calibrated against the C 1s signal (284.6 eV) of contaminant carbon. H_2 temperature-programmed reduction (H_2-TPR) was carried out in the RT −750 °C range on a Micromeritics AutoChem II 2920 instrument. About 100 mg of sample was placed in a U-shaped quartz tube, then treated in O_2 (40 mL/min) at 300 °C for 1 h, and finally cooled to RT before being reduced in a 5% H_2–95% He flow of 25 mL/min at a ramp of 10 °C/min. The thermal conductivity detector (TCD) responses were calibrated against that of the complete reduction of a standard CuO powdered sample (Aldrich, 99.995%).

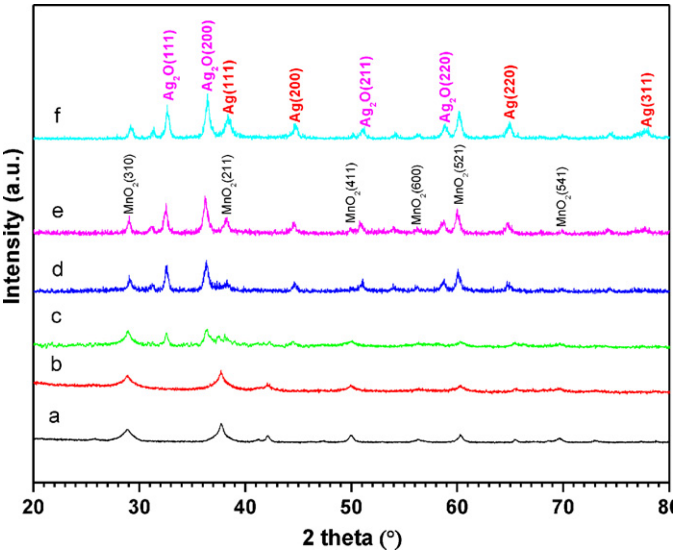

Fig. 1. The XRD patterns of *x*Ag/*nano*-MnO_2 with $x = 0$ (a), 1.0 wt% (b), 3.0 wt% (c), 5.0 wt% (d), 7.0 wt% (e), and 10.0 wt% (f).

2.3. Catalytic evaluation

Catalytic activity measurements of the samples for the oxidation of CO or benzene were carried out in a continuous flow fixed-bed quartz micro-reactor under atmospheric pressure. 100 mg of the catalyst (40–60 mesh) and 200 mg of quartz sand (40–60 mesh) were well mixed and loaded to the micro-reactor. The feed gas consisted of (1.08 vol% CO + air), the total flow rate was 100 mL/min, and the corresponding space velocity (SV) was 60,000 mL/(g h). Benzene was chosen as the representative VOC. A N_2 flow of 2.8 mL/min passed through a benzene-containing tubular saturator at 30 °C, and then mixed with an air flow of 197.2 mL/min, thus a SV value of 120,000 mL/(g h). In the feed gas mixture, the benzene vapor concentration was 2000 ppm. The effluent gases from the micro-reactor were analyzed on-line by a Shimadzu GC-14C gas chromatograph equipped with thermal conductivity detector (TCD) and a TDX-01 packing column for CO analysis or by a Techcomp GC-7900 gas chromatograph equipped with a flame ion detector (FID) and a SE-30 capillary column for organic compound analysis. The conversion of CO or benzene was calculated according to the change in CO or benzene concentrations in the inlet and outlet gas mixtures.

3. Results and discussion

3.1. Crystal phase composition

Fig. 1 shows the XRD patterns of the as-prepared manganese oxide and its supported Ag catalysts (*x*Ag/*nano*-MnO_2). For the manganese oxide support, 1Ag/*nano*-MnO_2, and 3Ag/*nano*-MnO_2, there were diffraction peaks in the 2θ range of 20–80° (Fig. 1(a)–(c)), ascribable to the tetragonal α-MnO_2 phase (JCPDS PDF# 44-0141). No significant signals assignable to Ag_2O or Ag phases were detected for the 1Ag/*nano*-MnO_2 and 3Ag/*nano*-MnO_2 catalysts. With the rise in Ag loading from 3.0 to 5.0 wt%, however, weak diffraction signals due to Ag_2O and Ag phases (Fig. 1(d)) appeared in the 5Ag/*nano*-MnO_2 catalyst. Further increasing Ag loading from 5.0 to 10.0 wt% resulted in the increase in amount of the Ag_2O and Ag phases. All of the XRD peaks due to the α-MnO_2, Ag_2O, and Ag phases could be well indexed, as indicated in Fig. 1(e) and (f). From Fig. 1, one can also observe that there was a difference in XRD peak intensity of these catalysts, indicating the presence of the α-MnO_2, Ag_2O, and Ag phases with different crystallinity.

3.2. Morphology and surface area

Representative TEM micrographs of the *nano*-MnO_2, 5Ag/*nano*-MnO_2, and 10Ag/*nano*-MnO_2 samples are shown in Fig. 2. There were a number of MnO_2 nanoparticles that were stacked together (Fig. 2(a)), the lattice spacings of α-MnO_2 could not be observed clearly, indicating that the α-MnO_2 phase was not good enough in crystallinity, in agreement with the result of XRD study (Fig. 1(a)). As shown in Fig. 1(b), the exposed lattice planes of α-MnO_2 were (2 0 0) and (3 1 0), corresponding to the *d* values of 0.49 and 0.31 nm that were not far away from those (0.489500 and 0.309300 nm, respectively) of the standard α-MnO_2 sample (JCPDS PDF# 44-0141). Comparing to the irregularly morphological *nano*-MnO_2 support (Fig. 2(a) and (b)), the *nano*-MnO_2 particles in 5Ag/*nano*-MnO_2 (Fig. 2(c) and (d)) and 10Ag/*nano*-MnO_2 (Fig. 2(e) and (f)) were sphere-like, with the particle sizes being in the range of 15–25 nm. The clearly aligned lattice fringes in the high-resolution TEM image of 5Ag/*nano*-MnO_2 (Fig. 2(d)) suggests that the Ag-loaded MnO_2 nanocrystallites possessed a good crystalline structure, a result possibly due to the second calcination treatment at 450 °C for 3 h after loading silver; in addition to the (3 1 0) plane of α-MnO_2, there was also detection of the exposed lattice planes (2 0 0) and (1 1 1) of Ag^0 and (1 1 1) of Ag_2O, which corresponded to the *d* values of 0.20, 0.24, and 0.27 nm, rather close to those (0.204000 and 0.236000 nm) of the standard Ag^0 (JCPDS PDF# 01-1167) sample and that (0.272000 nm) of the standard Ag_2O (JCPDS PDF# 01-1041) sample, respectively. Similar results were reported by other researchers [20]. The exposed lattice planes of α-MnO_2, Ag^0, and Ag_2O were also observed in the 10Ag/*nano*-MnO_2 sample (Fig. 2(f)). The above results reveal that there was co-presence of *nano*-MnO_2, Ag^0, and Ag_2O nanoparticles in the *x*Ag/*nano*-MnO_2 ($x = 5.0$ and 10.0 wt%) catalysts, which is consistent with the results of XRD investigations.

The BET surface areas of *nano*-MnO_2 and *x*Ag/*nano*-MnO_2 are listed in Table 1. It is clear that the *nano*-MnO_2 support showed a high surface area of 140 m^2/g. Loading 1.0 wt% Ag to *nano*-MnO_2 caused a little change in surface area of the obtained 1Ag/*nano*-MnO_2 catalyst. At an Ag loading of 3.0 or 5.0 wt%, the surface area decreased to 102–125 m^2/g. A further rise in Ag loading to more than 7.0 wt%, however, resulted in a significant drop in surface area (44–57 m^2/g) of the *x*Ag/*nano*-MnO_2 catalysts, which might be due to the aggregation of MnO_2 particles (Fig. 2) and the decrease of MnO_2 content in the supported catalysts.

3.3. Surface composition and oxidation state

XPS is a good tool to investigate the surface element compositions and metal oxidation states of a solid inorganic material. The XPS results of the *x*Ag/*nano*-MnO_2 catalysts are also summarized in Table 1. As revealed by the Ag 3d, Mn 2p, and O 1s core-level XPS spectra (not shown here) of *x*Ag/*nano*-MnO_2, the silver mainly existed in a highly dispersed Ag^0 domain on the surfaces of *nano*-MnO_2 at a lower gold loading ($x \leq 1.0$ wt%); when $x \geq 3.0$ wt%, the silver was present in the form of metallic Ag^0 clusters and dispersed Ag_2O domain, and the content of the former decreased at elevated silver loadings. The manganese on the *nano*-MnO_2 and *x*Ag/*nano*-MnO_2 surfaces existed in tri- and tetravalency, and the mean oxidation state of Mn increased with increasing silver loading. Based on the principle of electroneutrality, we hence deduce that oxygen vacancies might be present on/in *nano*-MnO_2 and its supported silver catalysts. The oxygen adspecies should dwell at the surface oxygen vacancies of *nano*-MnO_2 as well as the interface between the silver and *nano*-MnO_2. Such a deduction was substantiated by the O 1s XPS analysis of *x*Ag/*nano*-MnO_2. The loading of silver had significant effects on the molar ratios of surface adsorbed oxygen (O_{ads}) to lattice oxygen (O_{latt}) species and of surface Mn^{4+} to Mn^{3+} on *x*Ag/*nano*-MnO_2 (Table 1) through the interaction between Ag and *nano*-MnO_2. Similar effects have been also observed in the Ag/MnO_x–CeO_2 catalysts [21]. Usually, pure Ag_2O can decompose completely into metallic Ag^0 and O_2 at a calcination temperature of higher than 400 °C [22,23]. In the *x*Ag/*nano*-MnO_2 catalysts ($x = 5.0$–10.0 wt%) derived after calcination in air at 450 °C, however, there was presence of oxidized silver species (Ag_2O). The generation of Ag^+ species is an indication of strong interactions between silver and MnO_2, through which the active oxygen species adsorbed on the surface of MnO_2 could oxidize parts of Ag^0 into Ag^+. Therefore, the modifications in surface O_{ads}/O_{latt}, Mn^{4+}/Mn^{3+}, and Ag^+/Ag^0 molar ratios due to Ag loading and Ag–MnO_2 interactions would influence the catalytic behaviors of the *x*Ag/*nano*-MnO_2 materials for the oxidation of CO and benzene.

3.4. Reducibility

Fig. 3(A) illustrates the H_2-TPR profiles of the *x*Ag/*nano*-MnO_2 catalysts. In general, the reduction of MnO_2 follows a typical two-step process, i.e., $MnO_2 \rightarrow Mn_3O_4 \rightarrow MnO$ [24]. From Fig. 3A(a), one can observe two broad and weak reduction bands centered at 101 and 365 °C and one strong reduction band at 211 °C, corresponding to the reduction of $MnO_2 \rightarrow Mn_3O_4$ and $Mn_3O_4 \rightarrow MnO$ [24]. Due to the bigger negative reduction potential of MnO, no reduction band assignable to the $MnO \rightarrow Mn^0$ process was observed even up to 750 °C [24]. Therefore, it is reasonably deduced that MnO was the final state of *nano*-MnO_2 reduction, which was confirmed by the XRD results (not shown) of the *nano*-MnO_2 sample after the H_2-TPR experiment. For the *nano*-MnO_2 sample, the H/Mn molar ratio estimated from the amount of hydrogen consumed during the reduction process was ca. 1.58, lower than the theoretical H/Mn molar ratio (2.0) calculated according to the ($MnO_2 + H_2 \rightarrow MnO + H_2O$) reaction. This result implies that there was presence of Mn ions with mixed oxidation states (i.e., Mn^{3+} and Mn^{4+}), in good agreement with the results of XPS studies. Compared to the reduction behavior of the *nano*-MnO_2 support, the introduction of silver brought about remarkable alterations in position and shape of reduction bands and significant shifts of the reduction bands took place (Fig. 3A(b)–(f)). There were two weak bands at 112 and 232 °C and one strong band at 171 °C for the 1Ag/*nano*-MnO_2 catalyst, one weak band at 239 °C and two strong bands at 95 and 154 °C for the 3Ag/*nano*-MnO_2 catalyst, two strong bands at 80 and 144 °C for the 5Ag/*nano*-MnO_2 catalyst, one weak band at 85 °C and one strong band at 189 °C for the 7Ag/*nano*-MnO_2 catalyst, and one weak band at 84 °C and one strong band at 202 °C for the 10Ag/*nano*-MnO_2 catalyst. The reduction bands below 120 °C and in the range of 120–450 °C can be attributed to the $MnO_2 \rightarrow Mn_3O_4$ and $Mn_3O_4 \rightarrow MnO$ processes [24], respectively. Of course, the reduction of the small amount of silver oxide species occurred below 120 °C and their reduction bands might be overlapped with the first reduction band of *nano*-MnO_2 [24]. From the H_2-TPR profiles, one can readily see that the 5Ag/*nano*-MnO_2 catalyst was the most reducible at low temperatures. That is to say, at a silver loading of 5.0 wt%, the as-prepared nanocatalyst possessed the best reducibility. It is well-known that manganese oxides exhibit strong oxygen storage/release ability due to the fact that they easily undergo a rapid reduction–oxidation cycle through the interaction with reducing or oxidant agents, accompanying by the formation of manganese ions in various oxidation states (Mn^{2+}, Mn^{3+} or Mn^{4+}) [25]. An explanation on the lower reduction temperature of MnO_2 in the *x*Ag/*nano*-MnO_2 catalysts is that the noble metal (e.g., Ag) could enhance the reduction of MnO_2 to Mn^{3+} and/or Mn^{2+} via the spillover of active hydrogen species adsorbed

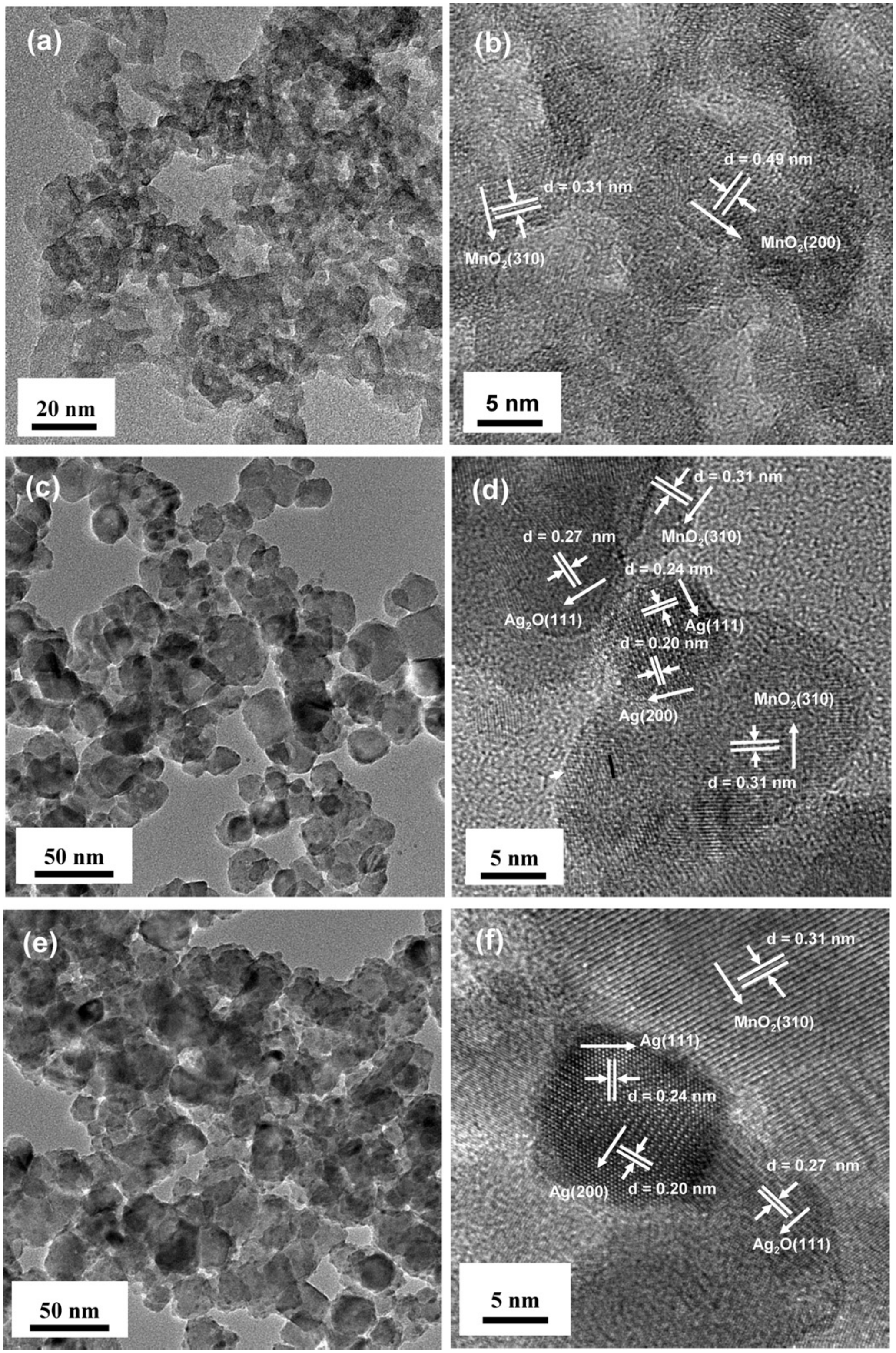

Fig. 2. TEM images of (a and b) *nano*-MnO_2, (c and d) 5Ag/*nano*-MnO_2, and (e and f) 10Ag/*nano*-MnO_2.

on the noble metal surface during the H_2-TPR experiments [26,27] or by promoting the mobility of lattice oxygen of MnO_2 [28]. From the H_2-TPR results, one can deduce that there might be existence of a strong interaction (i.e., synergistic action) between Ag and MnO_2 nanodomains. Such a deduction has also been confirmed by the results of Ag/MnO_2 nanowire/nanorods reported by Li and coworkers [29].

Although the H_2 consumption of the *x*Ag/*nano*-MnO_2 samples decreased with the rise in Ag loading (Table 1), their reducibility did not follow such a trend. It is a better method to compare the reducibility of catalysts in terms of the initial H_2 consumption rate per mole of reducible metal (Ag or Mn) where reduction is less than 20% (i.e., no occurrence of phase transformation). Fig. 3(B) shows the initial H_2 consumption

Table 1
Total BET surface areas, H_2 consumptions, binding energies of surface elements, and Mn^{4+}/Mn^{3+}, Ag^{+}/Ag^{0}, and O_{ads}/O_{latt} molar ratios of the *x*Ag/*nano*-MnO_2 catalysts.

x (wt%)	BET surface area (m^2/g)	H_2 consumption (mol_{H_2}/mol_{Mn})	Mn $2p_{3/2}$ (eV)		Mn^{4+}/Mn^{3+}	Ag $3d_{5/2}$ (eV)		Ag^{+}/Ag^{0}	O 1s (eV)		O_{ads}/O_{latt}
0	140	0.789	641.0	642.4	1.79	–	–	–	529.8	532.3	0.74
1.0	136	0.781	640.9	642.6	1.94	–	–	–	530.1	532.4	0.89
3.0	125	0.724	641.1	642.5	2.30	368.0	366.9	0.18	530.1	532.2	0.31
5.0	102	0.706	641.0	642.5	2.36	368.0	366.9	0.36	530.3	532.6	0.32
7.0	57	0.603	640.7	642.0	7.13	367.9	366.5	0.38	529.9	532.1	0.25
10.0	44	0.582	640.5	642.0	7.56	368.2	366.9	0.63	530.1	532.2	0.23

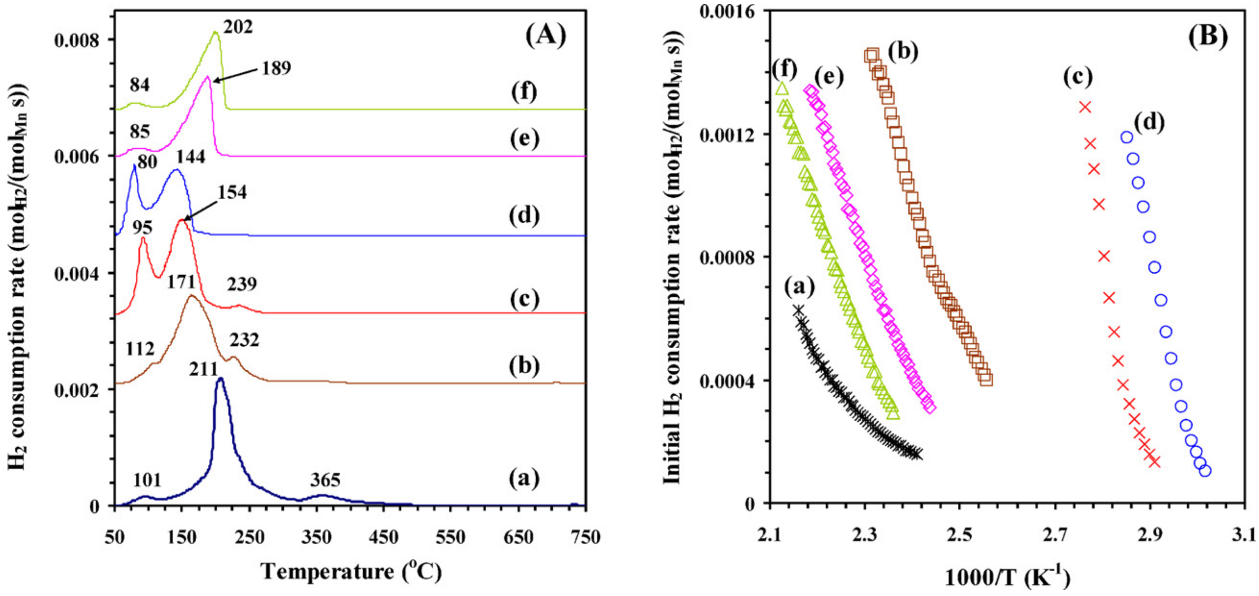

Fig. 3. (A) TPR profiles and (B) initial H_2 consumption rate versus inverse temperature of *x*Ag/*nano*-MnO_2 with *x* = 0 (a), 1.0 wt% (b), 3.0 wt% (c), 5.0 wt% (d), 7.0 wt% (e), and 10.0 wt% (f).

rates of the catalysts versus inverse temperature. Apparently, the initial H_2 consumption rate decreased in the order of 5Ag/*nano*-MnO_2 > 3Ag/*nano*-MnO_2 > 1Ag/*nano*-MnO_2 > 7Ag/*nano*-MnO_2 > 10Ag/*nano*-MnO_2 > *nano*-MnO_2, coinciding with the sequence of their catalytic performance (shown below).

3.5. *Catalytic performance*

Specific reaction rate (normalized by per mole of the reducible metal in the catalyst) can be used to evaluate the catalytic performance of a material. Fig. 4(A) and (C) shows the specific reaction rates normalized per mole of Ag and per mole of Mn of the *x*Ag/*nano*-MnO_2 catalysts for the oxidation of CO, respectively. It is observed that below 70 °C the specific CO reaction rates normalized by per mole of Ag of all the catalysts were lower, but above 70 °C they were significantly different and decreased at elevated Ag loadings, indicating that a lower Ag loading led to a higher Ag dispersion on *nano*-MnO_2, which would be favorable for the enhancement in catalytic activity; the specific CO reaction rates normalized by per mol of Mn of these catalysts, however, decreased in the order of 5Ag/*nano*-MnO_2 > 3Ag/*nano*-MnO_2 > 1Ag/*nano*-MnO_2 > *nano*-MnO_2 > 7Ag/*nano*-MnO_2 > 10Ag/*nano*-MnO_2. There was an obvious discrepancy in changing trend of specific reaction rates normalized by per of Ag and by per mole Mn of the catalysts. This result suggests that (i) an appropriate Ag loading was required for obtaining the highest catalytic performance in the low-temperature CO oxidation, and (ii) the excellent performance of the 5Ag/*nano*-MnO_2 catalyst might be also associated with the synergistic action between the silver (or silver oxide) and manganese oxide nanoparticles. Obviously, the optimal Ag loading for achieving the best catalytic performance was 5.0 wt%, giving a specific reaction rate of 2.18 $mol_{CO}/(mol_{Mn}\ h)$ with a corresponding CO conversion = 90% at ca. 83 °C. After investigating the oxidation of CO over the MnO_2-supported silver catalysts derived via an incipient wetness impregnation route, Li and coworkers [29] observed that the 15 wt% Ag/α-MnO_2 catalyst showed a specific reaction rate of ca. 1.51 $mol_{CO}/(mol_{Mn}\ h)$ with a corresponding CO conversion = 90% at ca. 90 °C, which was inferior to our catalyst 5Ag/*nano*-MnO_2.

Generally speaking, the oxidation of CO over transition-metal oxides (e.g., MnO_2, Co_3O_4, Fe_2O_3, and CuO) follows a Mars–van Krevelen mechanism, in which O_{latt} involves in CO oxidation and the reduced surface of the catalyst is re-oxidized by the gas-phase oxygen from the feed mixture [13]. For the supported silver catalysts in CO oxidation, although the detailed mechanisms are not completely understood, a viable reaction pathway might be: silver nanoparticles activate CO molecules, the support activates oxygen molecules, and the oxidation of CO occurs at the silver–support interface. As reported previously, TiO_2-supported nanosized gold catalysts were extremely active at low temperatures for CO oxidation, a result due to the formation of well-dispersed Au nanodomains [30]. In our case, the presence of Ag and/or Ag_2O nanodomains on the *nano*-MnO_2 support and the synergistic action between them gave rise to the excellent catalytic activity of 5Ag/*nano*-MnO_2. As pointed out by Imamura et al. [31], the catalytic activity of the Ag–Mn composite oxides for CO oxidation was dependent upon the interaction between the Ag and Mn. The active oxygen species over Ag were consumed mainly in the oxidation of CO, and the manganese oxide served as an oxygen carrier [19]. Moreover, a strong interaction would favor the spillover of oxygen species from Mn to Ag, hence improving the catalytic

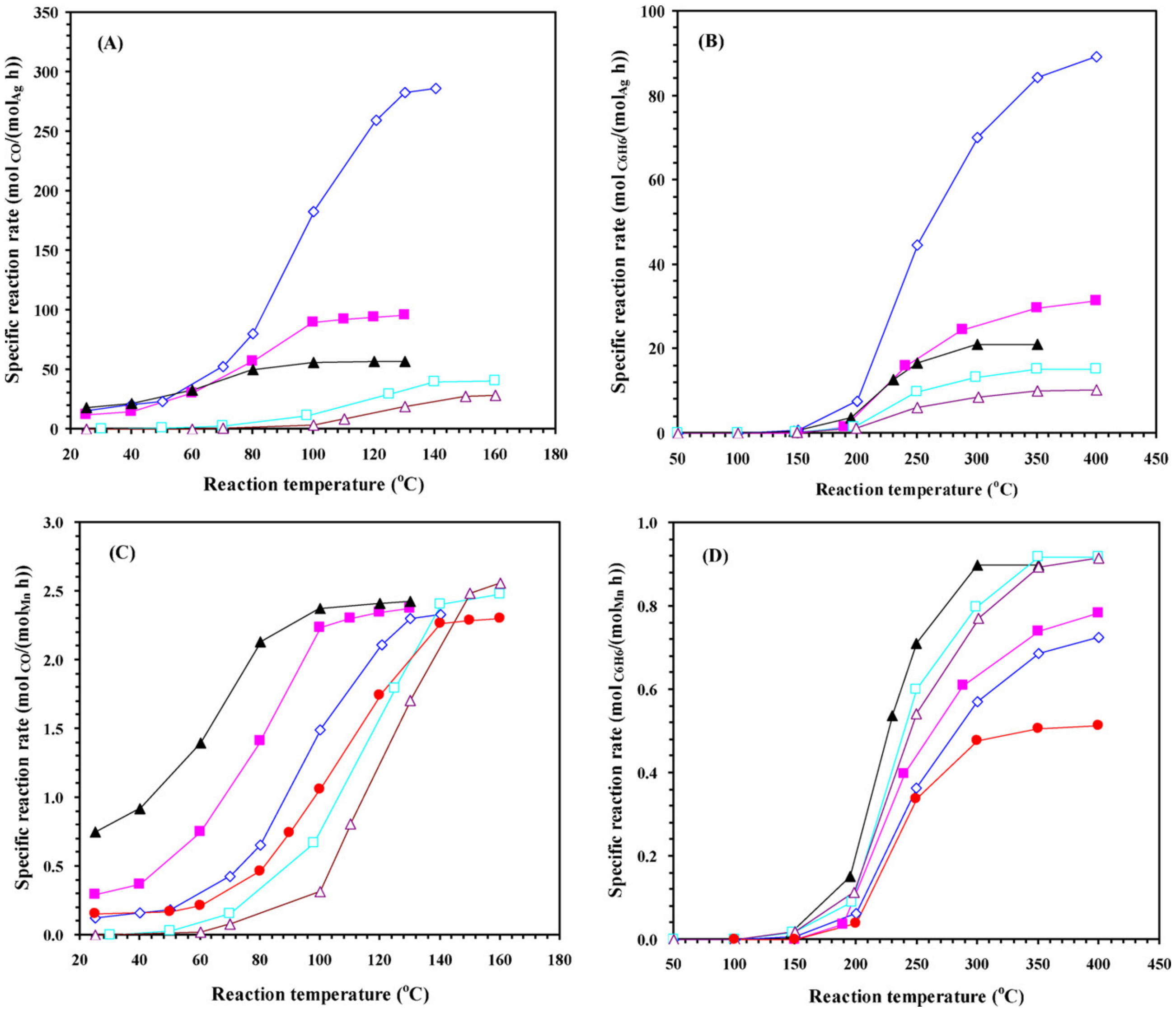

Fig. 4. Specific (A) CO and (B) benzene reaction rates normalized per mol of Ag and specific (C) CO and (D) benzene reaction rates normalized per mol of Mn as a function of reaction temperature at SV = 60,000 mL/(g h) for CO oxidation and 120,000 mL/(g h) for benzene oxidation over the *x*Ag/*nano*-MnO$_2$ catalysts with *x* = 0 (●), 1.0 wt% (◇), 3.0 wt% (■), 5.0 wt% (▲), 7.0 wt% (□), and 10 wt% (△).

activity. This is in good agreement with the H$_2$-TPR results, which demonstrated that the interaction between Ag and *nano*-MnO$_2$ lowered the reduction temperature of *nano*-MnO$_2$. Therefore, we believe that a strong metal–support interaction would also exist in the *x*Ag/*nano*-MnO$_2$ samples, which resulted in an enhanced catalytic activity. Similar results have also been reported in the Au/CeO$_2$ and Au/CuO catalyst systems [32]. Additionally, the excellent catalytic activity of 5Ag/*nano*-MnO$_2$ was also related to its higher O$_{latt}$ species concentration, as demonstrated by the results of XPS analysis (Table 1).

Among the VOCs, aromatics are believed to be relatively hard to be eliminated. We selected benzene as a representative of aromatics to examine the catalytic performance of *x*Ag/*nano*-MnO$_2$. Fig. 4(B) and (D) shows the specific reaction rates normalized per mole of Ag and per mole of Mn of the *x*Ag/*nano*-MnO$_2$ catalysts for the oxidation of benzene, respectively. CO$_2$ and H$_2$O were the only products formed. From Fig. 4(B), one can see that the specific reaction rate normalized per mole of Ag decreased with increasing the Ag loading, a changing trend similar to that for CO oxidation. As shown in Fig. 4(D), the pure *nano*-MnO$_2$ support was inferior in catalytic activity to the *x*Ag/*nano*-MnO$_2$ catalysts. This result indicates that silver supported on *nano*-MnO$_2$ played an important role for benzene oxidation. Over the *x*Ag/*nano*-MnO$_2$ catalysts, the activity increased with a rise in Ag loading from 1.0 to 5.0 wt%, then decreased with increasing Ag loading from 5.0 to 10.0 wt%. Like in the case of CO oxidation, the 5Ag/*nano*-MnO$_2$ catalyst performed the best in the oxidation of benzene.

Considering the catalytic performance of *x*Ag/*nano*-MnO$_2$ ($0 < x \leq 5$) better than that of the pure *nano*-MnO$_2$ support, we believe that the synergistic action between silver and *nano*-MnO$_2$ would be present and favor the significant enhancement in catalytic performance. In other words, the interface of silver and manganese oxide nanodomains might play an important role in improving the catalytic activity. It is probable that the presence of silver would cause a decrease in strength of the surface Mn–O bonds adjacent to silver nanodomains, leading to a higher mobility and reactivity of surface lattice oxygen, and hence enhancing the catalytic performance. After investigating the combustion of some VOCs over the Fe$_2$O$_3$-supported IB group metal (Cu, Ag or Au) catalysts, Scire et al. [33] pointed out that the IB metal could weaken the Fe–O bonds and the mobility of O$_{latt}$ was promoted as a result. In line with these observations, we tentatively propose that the combustion of benzene would take place not only on the surface of Ag nanodomains but also at the interface of Ag and MnO_2 nanodomains.

4. Conclusions

Nanometer α-MnO_2-supported Ag catalysts (xAg/*nano*-MnO_2) with $x = 0$–10.0 wt% could be prepared via the incipient wetness impregnation route. The introduction of Ag resulted in a drop in surface area of the catalyst. The Ag particles were highly dispersed on *nano*-MnO_2 at a lower Ag loading. For the xAg/*nano*-MnO_2 samples, the surface Mn^{4+}/Mn^{3+} atomic ratios increased but the surface O_{ads}/O_{latt} molar ratios decreased at elevated Ag loadings. Loading Ag could modify the reducibility of the xAg/*nano*-MnO_2 samples via the interaction between the Ag and MnO_2 nanodomains and the best reducibility was achieved at an Ag loading of 5.0 wt%. The loading of Ag on MnO_2 nanoparticles could alter the catalytic activities for the oxidation of CO and C_6H_6, with the best performance being obtained over the 5Ag/*nano*-MnO_2 catalyst. Such excellent catalytic performance was related to the highly dispersed Ag, good low-temperature reducibility, and synergistic action between the Ag and MnO_2 nanodomains.

Acknowledgements

This research was supported by National Natural Science Foundation of China (No. 20777005/B0703), Beijing Natural Science Foundation of China (No. 8082008) and Beijing Municipal Foundation for Excellent Person of Ability (No. 20071 D0501500210).

References

[1] R.J. Farrauto, R.M. Heck, Catal. Today 55 (2000) 179–187.
[2] M. Kosusko, C.M. Nunez, J. Air Waste Manage. Assoc. 40 (1990) 254–259.
[3] N. De, Nevers:, Air Pollution Control Engineering Civil Engineering Series, McGraw-Hill International Edition, 1995.
[4] F.I. Khan, A.K. Ghoshal, J. Loss Prev. Proc. Ind. 13 (2000) 527–545.
[5] J.J. Spivey, Ind. Eng. Chem. Res. 26 (1987) 2165–2180.
[6] S. Scirè, S. Minicò, C. Crisafulli, C. Satriano, A. Pistone, Appl. Catal. B 40 (2003) 43–49.
[7] P. Papaefthimiou, T. Ioannides, X.E. Verykios, Catal. Today 54 (1999) 81–92.
[8] W. Wang, H.B. Zhang, G.D. Lin, Z.T. Xiong, Appl. Catal. B 24 (2000) 219–232.
[9] J.J. Spivey, J.B. Butt, Catal. Today 11 (1992) 465–500.
[10] M.F.M. Zwinkels, S.G. Jaras, P.G. Menon, T.A. Griffin, Catal. Rev. – Sci. Eng. 35 (1993) 319–358.
[11] H. Chu, W.T. Lee, K.H. Horng, T.K. Tseng, J. Hazard. Mater. 82 (2001) 43–53.
[12] S.H. Taylor, C.S. Heneghan, G.J. Hutchings, I.D. Hudson, Catal. Today 59 (2000) 249–259.
[13] S.K. Kulshreshtha, M.M. Gadgil, Appl. Catal. B 11 (1997) 291–305.
[14] M.F. Luo, B. Zhou, X.X. Yuan, Chem. World 34 (1993) 278–281 (in Chinese).
[15] G.B. Hoflund, S.D. Gardner, D.R. Schryer, B.T. Upchurch, E.J. Kielin, Appl. Catal. B 6 (1995) 117–126.
[16] L.C. Wang, L. He, Q. Liu, Y.M. Liu, M. Chen, Y. Cao, H.Y. He, K.N. Fan, Appl. Catal. A 344 (2008) 150–157.
[17] J.G. Serafin, A.C. Liu, S.R. Seyedmonir, J. Mol. Catal. A 131 (1998) 157–168.
[18] M.F. Luo, X.X. Yuan, X.M. Zheng, Appl. Catal. A 175 (1998) 121–129.
[19] E.M. Cordi, J.L. Falconer, Appl. Catal. A 151 (1997) 179–191.
[20] M. Jin, X. Zhang, S. Nishimoto, Z.D. Liu, A. Tryk, T. Murakami, A. Fujishima, Nanotechnology 18 (2007) 075605.
[21] X. Tang, J. Chen, Y. Li, Y. Li, Y. Xu, W. Shen, Chem. Eng. J. 118 (2006) 119–125.
[22] J.F. Weaver, G.B. Hoflund, J. Phys. Chem. 98 (1994) 8519–8524.
[23] G.I.N. Waterhouse, G.A. Bowmaker, J.B. Metson, Phys. Chem. Chem. Phys. 3 (2001) 3838–3845.
[24] J. Carno, M. Ferradon, E. Bjornbom, S. Jaras, Appl. Catal. A 155 (1997) 265–281.
[25] Y.F. Chang, J.G. McCarty, Catal. Today 30 (1996) 163–170.
[26] H.E.J. van't Blik, D.C. Koningsberger, R. Prins, J. Catal. 97 (1986) 210–218.
[27] J.M. Rynkowski, T. Paryjczak, M. Lenik, Appl. Catal. A 126 (1995) 257–271.
[28] Y. Tsuji, S. Imamura, in: T. Inui, et al. (Eds.), New Aspects of Spillover Effect in Catalysis, vol. 77, Elsevier, Amsterdam, 1993, pp. 405–408.
[29] R. Xu, X. Wang, D. Wang, K. Zhou, Y. Li, J. Catal. 237 (2006) 426–430.
[30] M. Haruta, Cattech 6 (2002) 102–115.
[31] S. Imamura, H. Sawada, K. Uemura, S. Ishida, J. Catal. 109 (1988) 198–205.
[32] A.M. Venezia, G. Pantaleo, A. Longo, G.D. Carlo, M.P. Casaletto, F.L. Liotta, G. Deganello, J. Phys. Chem. B 109 (2005) 2821–2827.
[33] S. Scire, S. Minico, C. Crisofulli, S. Galvano, Catal. Commun. 2 (2001) 229–232.